Astron. Astrophys. 331, 52–60 (1998)

ASTRONOMY
AND
ASTROPHYSICS

Flared dust disks and the IR emission of AGN

V. Manske, Th. Henning, and A.B. Men'shchikov

Astrophysical Institute and University Observatory, Schillergäßchen 3, D-07745 Jena, Germany
(manske@astro.uni-jena.de, henning@astro.uni-jena.de, sascha@astro.uni-jena.de)

Received 12 November 1996 / Accepted 17 October 1997

Abstract. We describe an accelerated version of the two-dimensional (2D) ray-tracing code for radiative transfer in disk configurations developed by Men'shchikov & Henning (1997). This new code enabled us to perform an extensive scan of the parameter space of flared dust disks around active galactic nuclei (AGN). Among the parameters influencing spectral energy distributions, we varied the dust model, the density distribution, the opening angle, and the optical depth of the disks as well as the anisotropy of the radiation field of the central source. Our aim was to find configurations that produce continuum spectra similar to the observed ones which show no 10μm emission feature along lines of sight where the central source is not obscured.

We found that optically thick disks in combination with a strong anisotropic 7 radiation source can produce such spectral energy distributions. The best-fit models show a very high optical depth of $\tau_{200\mathrm{nm}} \approx 1000$ (along the equatorial plane), an opening angle of 90°, and a density distribution proportional to r^{-1}.

As the strong anisotropy of the source radiation prevents significant silicate emission features from appearing, we see no need for the depletion of silicate grains by shocks or for the presence of compact cores.

Key words: radiative transfer – dust: extinction – infrared: galaxies – quasars: general – galaxies: ISM

1. Introduction

In the standard classification scheme, active galactic nuclei (AGN) are divided into radio-loud and radio-quiet objects appearing in elliptical or spiral host galaxies, correspondingly. They are subdivided into narrow-line and broad-line AGN if they show either narrow emission-line regions (NLR) or NLR plus broad emission-line regions (BLR) (see review by Lawrence 1987). Almost all known types of active galaxies, such as Seyfert galaxies, Markarians, quasars, and Fanaroff-Riley galaxies, fit into this scheme.

First attempts to explain the differences between Seyfert galaxies of type 1 and 2 (see Lawrence & Elvis 1982) already contained the main aspects of the modern unified theory of broad-line and narrow-line AGN. According to this theory, major differences between narrow-line and broad-line AGN depend on occultation of the central source (viewing angle effects) and on their actual evolutionary state. The engine which drives the AGN is supposed to be an accreting black hole (Rees 1984) which accounts for jets and radio lobes and which is surrounded by a dusty molecular torus. Detailed discussions of the unified theory can be found in the reviews by Lawrence (1987), Antonucci (1993), and Urry & Padovani (1995).

The discovery of broad emission lines in the polarized spectra of narrow-line AGN gave first strong support to this picture (Antonucci & Miller 1985, Miller & Goodrich 1990, Tran 1995). Other authors found polarized light reflected off dust clouds on scales of $\sim$ 100 pc (Miller et al. 1991, Scarrott et al. 1991), evidence for dust tori (Storchi–Bergmann et al. 1992), and dust in the outer parts of BLR (Goodrich 1995). Recent Hubble Space Telescope observations directly confirmed the existence of a dust torus in NGC 4261 (Jaffe et al. 1993) and gave strong evidence for the presence of a black hole in M87 (Harms et al. 1994).

In the last few years, the development of two-dimensional (2D) radiative transfer codes enabled several authors to investigate spectral properties of the AGN dust tori. Pier & Krolik (1992, 1993) found good agreement with observations using cylindrical models for the dust tori. Granato & Danese (1994) investigated in detail the influence of parameters of a torus on the 10μm silicate feature. Efstathiou & Rowan–Robinson (1995) concluded that tapered disks explain the observed data better than flared disks. Recently, Stenholm (1995) investigated flared and tapered disk models with a 3D code using Planck mean opacities to determine the temperature structure of the dust disks.

One major problem in modeling the AGN dust tori is to avoid the 10μm silicate emission feature for face-on lines of sight because analysis of the spectra of IRAS galaxies (Roche et al. 1991) and quasars (Sanders et al. 1989) showed that most face-on objects such as Seyfert 1 galaxies and quasars show featureless spectra.

In this paper, we will show that one can solve this problem simply by using a more realistic model to describe the central

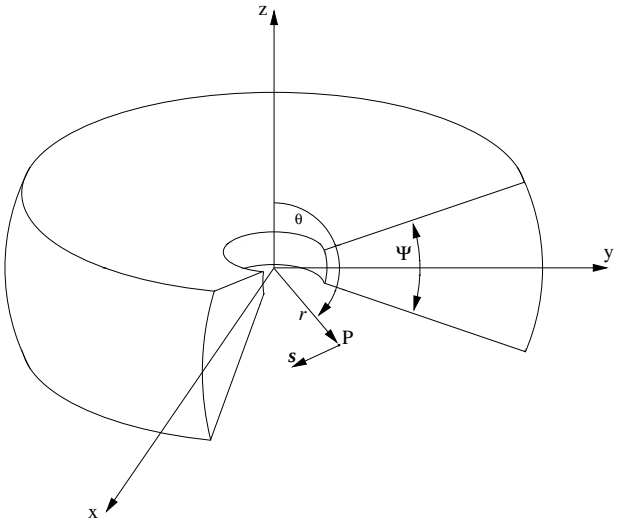

Fig. 1. Geometry of the model disk with the opening angle Ψ

energy source of the AGN. We see no strong need to introduce compact cores (Pier & Krolik 1993) or to invoke silicate grain depletion by shocks or hard radiation (Granato & Danese 1994, Laor & Draine 1993) in order to explain the observations.

In Sect. 2, we describe computational details of our model and improvements used to accelerate the computer code and to increase its accuracy. In Sect. 3, we describe the physical model used for our calculations and the parameter space we investigated. In Sect. 4, we present our results and discuss some of their aspects. Sect. 5 summarizes our conclusions.

In some sections of this paper, terminology problems could occur concerning the outer flared dust disk and the inner gas accretion disk. To avoid these conflicts, we usually refer to the flared dust disk as to the dust torus.

2. Computational method

Solving the 2D radiative transfer problem for a disk geometry is a challenge, in general, because of its high dimensionality.

We restrict ourselves to a flared-disk geometry. The specific intensity I_ν of the radiation field at any point P in the disk is a function of 5 parameters: the frequency ν, the position (r, θ), and the direction of light propagation $\boldsymbol{s}$ (Fig. 1). The disk itself is essentially a part of a sphere with two polar cones removed.

2.1. Radiative transfer

An approximate, very efficient method of the solution of the radiative transfer equation for flared disks was described by Men'shchikov & Henning (1997, hereafter MH). The main assumption of this method is that the density in the flared disk only depends on the radial coordinate. In addition, mean intensities and temperatures are calculated for points in the disk's midplane and at its upper and lower conical surfaces only. Below we give a brief summary of the method (see MH for details):

1. A set of cross sections of the disk is generated. The cross sections pass through the center of the coordinate system and have different inclinations to the equatorial plane of the disk. This enables the ϕ integration (see Eq. (4) below).

2. In each cross section, a set of rays with different impact parameters p is defined, for each radial point at the midplane and at the surface of the disk. This enables the θ integration in Eq. (4).

3. Along each ray, the one-dimensional (1D) equation of radiative transfer
$$\mu \frac{\mathrm{d}I_\nu(r,\mu)}{\mathrm{d}s} = -\sigma^{\mathrm{ext}}(\nu)\,[I_\nu - S_\nu] \tag{1}$$
is solved. Here r is the radial position, $\boldsymbol{s}$ is the direction of the ray, and $\mu = \pm\sqrt{1-p^2/r^2}$. Assuming isotropic scattering, the source function is defined by:
$$S_\nu = \frac{1}{\sigma(\nu)^{\mathrm{ext}}} \sum_{i,k} \left[\sigma(\nu)^{\mathrm{abs}}_{i,k}\, B_\nu(T_{i,k}) + \sigma(\nu)^{\mathrm{sca}}_{i,k}\, J_\nu\right], \tag{2}$$
where J_ν is the mean intensity, B_ν is the Planck function and $T_{i,k}$ is the temperature of the dust grains of the chemically distinct dust component i and the size bin k. The quantities $\sigma(\nu)^{\mathrm{abs}}_{i,k}$ and $\sigma(\nu)^{\mathrm{sca}}_{i,k}$ are the absorption and scattering coefficients of the dust component (i,k), and $\sigma(\nu)^{\mathrm{ext}}$ is the total extinction coefficient, defined by:
$$\sigma(\nu)^{\mathrm{ext}} = \sum_{i,k} \left[\sigma(\nu)^{\mathrm{abs}}_{i,k} + \sigma(\nu)^{\mathrm{sca}}_{i,k}\right] . \tag{3}$$

4. For all radial points at the disk's midplane and at its surface, the mean intensities and "new" dust temperatures are determined by:
$$J_\nu = \frac{1}{4\pi} \int_0^{2\pi} \int_0^{\pi} I_\nu(\phi,\theta) \sin\theta \,\mathrm{d}\theta \,\mathrm{d}\phi \tag{4}$$
$$\int_0^\infty \sigma(\nu)^{\mathrm{abs}}_{i,k}\, J_\nu \,\mathrm{d}\nu = \int_0^\infty \sigma(\nu)^{\mathrm{abs}}_{i,k}\, B_\nu(T_{i,k}) \,\mathrm{d}\nu . \tag{5}$$

The steps 3 and 4 are iterated until the temperature corrections fall below a certain small value at all points in the disk. An additional ray tracing along a given line of sight is performed to calculate spectral energy distributions (SEDs) and intensity maps. Typically, about 6 to 8 iterations are necessary for convergence depending on model parameters.

2.2. Improvements

Existing ray tracing codes have usually numerical problems for high optical depths which prove to be necessary for an investigation of the properties of dust tori around AGN. For extremely high optical depths, using only a moderate number of radial points (up to 100) may lead to large violations of energy conservation, due to numerical errors from solving the discretized and linearized version of Eq. (1). The usual recipe to avoid this problem is to increase the number of radial points, an extremely expensive way in terms of computation time (Table 3).

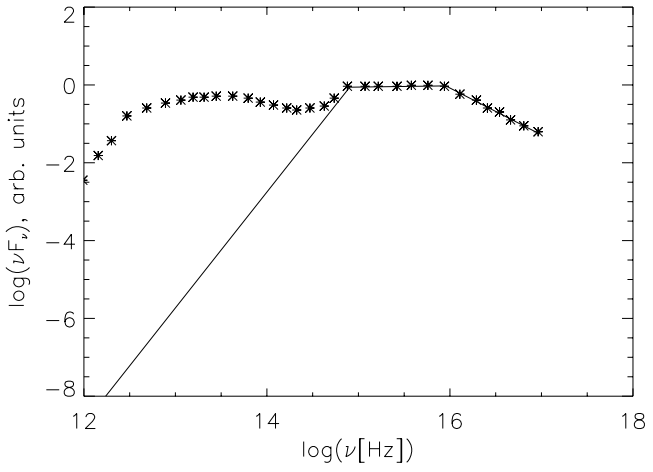

Fig. 2. The solid line shows the spectrum of the central source used for our calculations and the asterisks show the average observed spectrum of radio-quiet quasars from Sanders et al. (1989). The flux νF_ν, as a function of frequency ν, is plotted in arbitrary units.

To overcome these difficulties, we modified both the construction of the radial grid (adapting it to the optical depth) and the ray-tracing algorithm. Together with improvements of the numerical integration method, these modifications increased numerical accuracy and accelerated the code. In several test runs, the modified code has been found to be up to 15 times faster than the original MH code, mainly due to a smaller number of radial points. Details of the modifications and of the comparisons between the two codes are described in the Appendix.

3. The model

3.1. Central energy source

Following Stenholm (1995), we use a spectral energy distribution of the central source (see Fig. 2), which is based on observations of radio-quiet quasars (Sanders et al. 1989). For the infrared (IR) part of the source spectrum, a Rayleigh-Jeans extension of the thermal optical emission is used (Fig. 2, solid line), assuming that the optical to IR part of the source spectrum is blackbody like. The luminosity of the central source is set to $L_{\rm Source} = 10^{12} {\rm L}_\odot$ to be in agreement with the calculations of Sanders et al. (1989) and Stenholm (1995).

To investigate the effect of anisotropy of the radiation field of the central source we used two different kinds of central sources:

1. An *isotropic source* which is characterized by its luminosity $L_\star = L_{\rm Source}$ and its radius (0.1 pc).

2. An *anisotropic source* which consists of two components:
   (a) a compact spherical component with a luminosity of $L_\star = L_{\rm Source}$ and a radius of 0.001 pc,
   (b) a dust-free accretion disk with a luminosity of $L_{\rm acc}$ and a radius of 0.1 pc.

For the accretion disk we had to define the frequency dependence and the angular dependence of its radiation field. For the frequency dependence of the disk radiation, we used the same spectral energy distribution as for the isotropic central source (Fig. 2). This very simple approach enables us to compare directly the model SEDs obtained using both kinds of sources and it eases the comparison of the model SEDs with the observations because in our models the central source is always seen by an observer (next section).

As our code treats only spherically symmetric central sources, the definition of the angular dependence of the radiation field is not straightforward. We substitute the accretion disk by an equivalent sphere, having the same radius (0.1 pc), luminosity ($L_{\rm Sph} = L_{\rm acc}$), and spectral distribution of radiation $I_\nu^{\rm Sph}$. The flux $F_\nu^{\rm acc}(r,\theta)$ from the disk at the position (r,θ) depends on the area of the disk surface projected to a plane perpendicular to the line connecting this position with the disk ($\propto \cos\theta$). We replace the isotropic radiation of the equivalent sphere by:

$$F_\nu^{\rm acc}(r,\theta) = 2\,\cos\theta\, F_\nu^{\rm Sph}(r)\,, \tag{6}$$

where $F_\nu^{\rm Sph}(r)$ denotes the flux from the equivalent sphere. This leads to the equation for the corresponding intensities (at locations outside the source):

$$I_\nu^{\rm acc}(\theta) = 2\,\cos\theta\, I_\nu^{\rm Sph}\,. \tag{7}$$

Adding the specific intensity $I_\nu^\star$ of the compact isotropic component (Item 2a, above), the radiation field of the anisotropic central source is described by:

$$I_\nu^{\rm Source}(\theta) = 2\,\cos\theta\, I_\nu^{\rm Sph} + I_\nu^\star\,. \tag{8}$$

Introducing the "anisotropy parameter" γ defined by

$$L_{\rm acc} = \gamma L_\star\,, \tag{9}$$

we express the specific intensity of the anisotropic central source as follows

$$I_\nu^{\rm Source}(\theta) = [\,2\,\gamma\,\cos\theta + 1\,]\; I_\nu^\star\,. \tag{10}$$

3.2. Density distributions

We could use quite complicated parameterizations to describe the density distribution in our models (see, e.g. MH). However, in order to avoid additional free parameters and for the sake of a better comparison with the results of other authors, we adopted simple power-law density distributions:

$$\rho(r) \propto r^{-\beta}\quad,\qquad R_{\rm min} \le r \le R_{\rm max} \tag{11}$$

in our work. The outer radius $R_{\rm max}$ of the dust torus is set to 100 pc consistent with recent observations of NGC 4261 (Jaffe et al. 1993) and NGC 1068 (Young et al. 1996). Because this is not a well constrained parameter for quasars, we also calculated models for $R_{\rm max}$ = 50 and 200pc. However, it turned out that changing the outer radius within this interval, while keeping the

Table 1. Parameters of the dust models. Si: Silicate, G: Graphite. Radii: $a_{\rm min}$ and $a_{\rm max}$ in μm of the grain size distribution: $n(a) \propto a^{-q}$, $a_{\rm min} \leq a \leq a_{\rm max}$

No	Material	Radii [μm]	q
1	Si	0.1	–
2	Si + G	0.005 – 0.25	3.5
3	Si + G	0.01 – 1.0	3.5
4	Si + G	0.05 – 5.0	3.5

optical depth constant, has no big influence on the model SEDs. Therefore, we use the value of 100pc throughout this paper.

The inner radius $R_{\rm min}$ depends on the sublimation temperatures of the dust grains; it may be determined by other grain destruction processes as well. To simplify matters, we have chosen the same sublimation temperature of 1500 K for the silicate and carbon grains. This results in a value for the inner radius of the torus of about 1 pc.

The inner radius of the torus was fixed to the same value for the midplane and the surface of the torus. The fact that the surface is irradiated directly by the central source leads to significantly different temperatures at the surface and in the midplane. Therefore, the midplane temperature at the inner boundary of the torus is somewhat below and the surface temperature is above 1500 K. The deviations reach sometimes a few hundred K, especially for the models with a strongly anisotropic central source.

3.3. Dust models

In a detailed modeling, one might have to use dust mixtures consisting of amorphous carbon and silicate grains as well as grains with ice mantles (Men'shchikov & Henning 1997). These should correspond to the physical conditions in the objects which are studied, e.g., dense molecular cloud cores (Ossenkopf & Henning 1994, Preibisch et al. 1993, Henning et al. 1995), protostellar envelopes (Lenzuni et al. 1995) or protoplanetary accretion disks (Henning & Stognienko 1996). For silicates, recent optical data measured for cosmic dust analogues (Jäger et al. 1994, Dorschner et al. 1995) are available. However, for the sake of a better comparison with the results of other authors, we used the optical constants of the silicate and graphite dust from Draine (1985) in this work. Applying Mie theory, we calculated the coefficients of absorption and scattering for compact spherical grains.

Table 1 shows the parameters of the four dust models used in this work. For the composite dust models, we assume a mass ratio of silicate to carbon of 1:1. The power-law index q of the grain size distribution

$$n(a) \propto a^{-q} \,, \qquad a_{\rm min} \leq a \leq a_{\rm max} \tag{12}$$

is based on the results of Mathis et al. (1977, MRN). However, to account for possible aggregation effects and coagulation in the dense dust torus, we used larger size limits for the dust models no. 3 and 4.

Dust model 1 is only used in the first parts of our discussion, to allow the study of the influence of other parameters and the comparison of our results with those reported by Stenholm (1995). Dust model 4 is considered to illustrate the effect of grain size distribution. For any detailed modeling in this paper, we used the more realistic dust models no. 2 and 3. Dust model 2 is the classical MRN dust model with the optical constants from Draine (1985). Using the MRN dust causes one problem as grains smaller than 0.01 μm undergo temperature fluctuations. Therefore, they must be treated in a different way as larger grains (Guhathakurta & Draine 1989, and references therein). However, in our calculations we treated the small grains the same way as the larger ones. The effect of the temperature fluctuations will be investigated in a subsequent paper. To avoid this problem, the dust models 3 and 4 contain only grains with radii larger then 0.01 μm. The larger size limits in model 3 and 4 are inspired by the results of Fischer (1995) and Gledhill et al. (1996), who investigated dust disks around young stars, and by the dust model of Rowan-Robinson (1992). The latter one includes also very large grains of radii up to 30μm.

Table 2. "Grid points" of the models in the disk parameter space

Parameter	Values
$\tau_{\rm 200nm}$	1000, 500, 200, 100, 50, 20
γ	0, 0.3, 1, 3, 6
β	0.0, 0.5, 1.0, 1.5, 2.0
Ψ	120, 90, 50, 30

3.4. Calculations

We calculated more than 600 models to investigate the different regions of the multi-dimensional parameter space spanned by the model parameters summarized in Table 2.

The spectral energy distributions (SEDs) for some of these models, for a line of sight with a viewing angle of 84° above the torus midplane, are presented and discussed in the next section. The viewing angle is always larger than one-half of the opening angle of the model tori and, therefore, the central source can be seen directly by an observer. The value of 84° was chosen for the sake of comparison with the results reported by Stenholm (1995).

All models were calculated using 36 frequencies, equidistantly spaced in logarithms. The corresponding wavelength coverage ranges from 10 nm to 1 mm. Depending on the optical depth and the density gradient of the model, 48 to 65 radial points were necessary to reach the desired level of numerical accuracy (see the Appendix for details). Thus, the average CPU time for one model was about 30 min on a DEC-Alpha 3000/500 workstation.

4. Results and discussion

4.1. General remarks

At the beginning of this section, we want to make a few general comments related to the comparison of the theoretical results with the observations.

1. We would like to remind the reader that the overall problem in modeling the IR emission of quasars (or Seyfert 1 nuclei) is to produce SEDs showing no silicate emission feature at 10μm *and* having an UV to IR flux ratio that is in agreement with the observations.
2. As the spectrum of the central source is strongly dominated by UV-radiation, we use $\tau_{200\mathrm{nm}}$ instead of $\tau_{550\mathrm{nm}}$ to characterize our models.
3. For the sake of presentation, all SEDs with fluxes νF_ν are shown in arbitrary units as a function of frequency ν. They were scaled to the UV flux level of the average observed quasar spectrum from Sanders et al. (1989).
4. Almost all model spectra show a dip in the wavelength region of $\lambda \approx 1\mu$m ($\log(\nu/\mathrm{Hz}) \approx 14.4$) which is too deep compared with the observations. This discrepancy is probably caused by the simplicity of our model assumptions (structure of the configuration, no disk atmosphere; see Sect. 3). In addition, the emission of transiently-heated, very small dust grains ($a \leq 10$ nm) may fill up the observed gap. The modeling of the IR emission of the star-burst galaxy M82 with a 1D radiative transfer code by Krügel & Siebenmorgen (1994) indicate the viability of such an effect. Models including transiently heated particles will be presented in a subsequent paper.
5. The small bump, seen in some of the SEDs around $\nu = 10^{15}$Hz ($\lambda \approx 300$nm), is radiation from the central source scattered by small silicate grains, reflecting the peak of their albedo around 300 nm. However, this bump vanishes naturally if the other dust models are used (see Fig. 3).

4.2. Models with isotropic central sources

In this section, we give only a brief summary of the results we obtained using isotropically radiating central sources, because they mostly confirm results published by other authors. For a "quick look", we refer to the results shown in Fig. 3.

Almost every combination of model parameters (Table 2) led to a SED which was inconsistent with the observed data. The model SEDs showed at least one of the following discrepancies:

1. The silicate feature appeared in emission. This was frequently seen in SEDs of dust tori with low optical depth ($\tau_{200\mathrm{nm}} < 100$, see Fig. 3) and in SEDs of dust tori with constant density.
2. The silicate feature tends to appear in absorption. This occured sometimes if the optical depth was very high ($\tau_{200\mathrm{nm}} \geq 100$), especially if steep density distributions ($\beta = 2$) were used.
3. The model SED showed infrared flux values that were inconsistent with the observations of Sanders et al. (1989). This effect was found to be independent of the dust model (Fig. 3) that was used.

Only tori with opening angles below 90° produced almost featureless SEDs with an infrared to UV flux ratio that was in agreement with the observed data. But these model are very unrealistic because statistical analysis concerning the relative

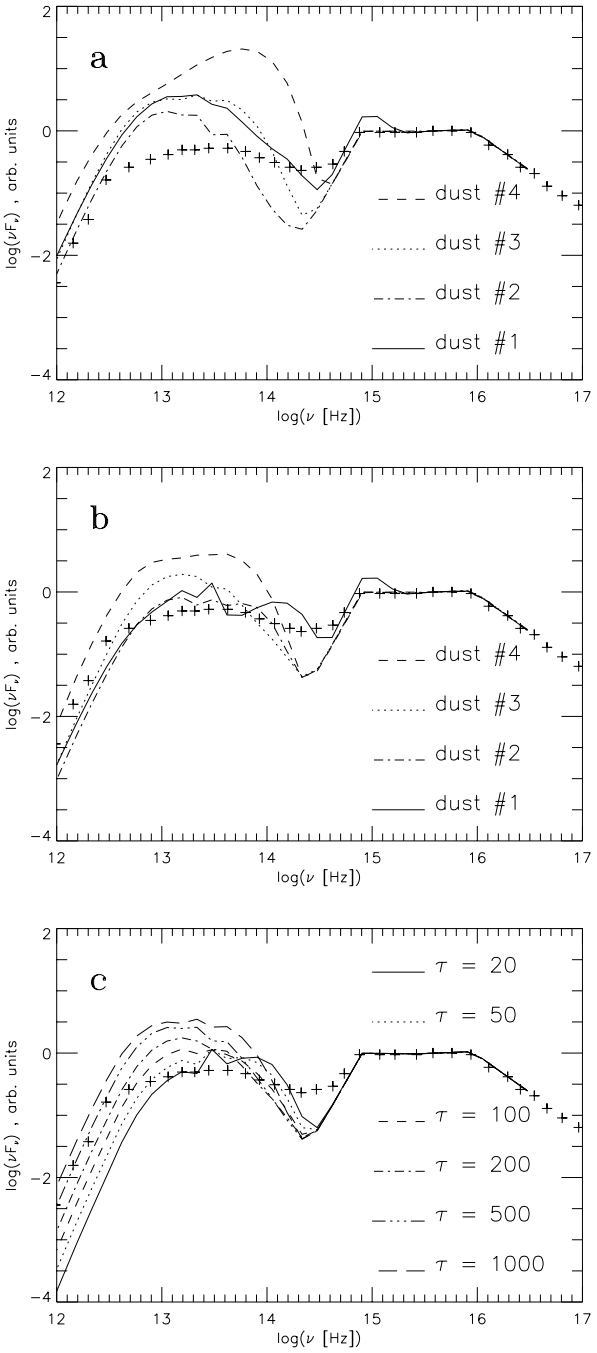

Fig. 3a–c. Face-on SEDs for dust tori with an opening angle of $\Psi = 120°$ and a medium density gradient $\beta = 1$ using the isotropic radiation source. **a** effect of dust model for tori with $\tau_{200\mathrm{nm}} = 1000$. **b** effect of dust model for tori with $\tau_{200\mathrm{nm}} = 200$. **c** effect of optical depth for tori using dust model no. 3. The '+' signs indicate the observed data from Sanders et al. (1989). For reference, the silicate feature appears at $10\mu\mathrm{m} \approx log(\nu) = 13.4$

numbers of Seyfert galaxies of type 1 and type 2 (Heckman 1995) and of narrow-line to broad-line AGN (Lawrence 1991) indicate that tori opening angles are larger than 90°.

The fact that other authors found dust tori models which fitted the observed data seems to have simple explanations. First, almost all published models used dust tori with a slightly different geometry. The tori were either cylindrically saped (Pier & Krolik 1992, Granato & Danese 1994) or had a tapered disk geometry (Efstathiou & Rowan-Robinson 1995, Stenholm 1995). This different shape leads to a lower illumination of the tori surface, and, therefore, to less IR emission. Second, somewhat different dust models were used. Granato & Danese (1994) used dust that was depleted in small silicates to suppress the silicate emission, whereas Stenholm (1995) used Planck-mean opacities. But already Preibisch et al. (1995) showed that in gray radiative transfer models temperatures are often underestimated which naturally leads to lower thermal IR fluxes.

Therefore, we conclude that as far as our investigated parameter space is concerned, models of dust tori with flared disk geometry, an isotropic central source, dust composed of silicate and graphite grains, and simple power-law density distributions fail to explain the observed featureless AGN spectra: the models we investigated can produce featureless spectra but then they produce always too high IR to UV flux ratios, in contrast to the observations.

However, in the next section we show that the use of anisotropically radiating central sources can solve the problems which were discussed above.

4.3. Models with anisotropic sources

In Fig. 4 we show some of the spectra obtained using an anisotropic central source (see Sect. 3.1). We present only models with a moderate density gradient (β = 1) because our calculations showed that such tori models give reasonable fits to the observations. The change of the source radiation field produces two major effects:

1. In all SEDs for the $\gamma \geq 1$ models, the UV flux is significantly higher than the IR flux, in agreement with the observations. The reason is that the disk component of the central source radiates much more into the line of sight compared to the isotropic source (Eqs. (6), (10)). On the other hand, this leads to a lower irradiation of the body of the torus and, therefore, to lower dust temperatures. As a consequence, we obtain an increase of the flux ratio between the UV and the (thermal) IR parts of the emitted continuum.

2. None of the SEDs in Fig. 4 shows a silicate emission feature, like all other model SEDs we obtained for tori with high optical depth using the anisotropic sources. As described above, the temperature distribution in the model torus changes if an anisotropically radiating source is used. Therefore, it is necessary to increase the mass of dust, and thus the optical depth, to reproduce the observed UV to IR flux ratio, wheras tori with the same optical depth using isotropic sources show allways too much IR emission. On the one hand, the high optical depth ($\tau_{200\mathrm{nm}}$ = 3000) prevents the silicate feature from appearing in emission. On the other hand, with anisotropic sources the dust temperatures at the conical surface of the torus are higher compared to those obtained with isotropic sources. Hence, the silicate emission from the dust at the conical surface can fill up any absorption feature that tends to appear in the SEDs for tori with very high optical depth using isotropic sources (Fig. 3). Even some models with an isotropic source (Fig. 3a) produce featureless SEDs if the optical depth is very high, but then the IR flux is much higher than observed. If anisotropically radiating sources are used it is not necessary to deplete the silicate content of the dust.

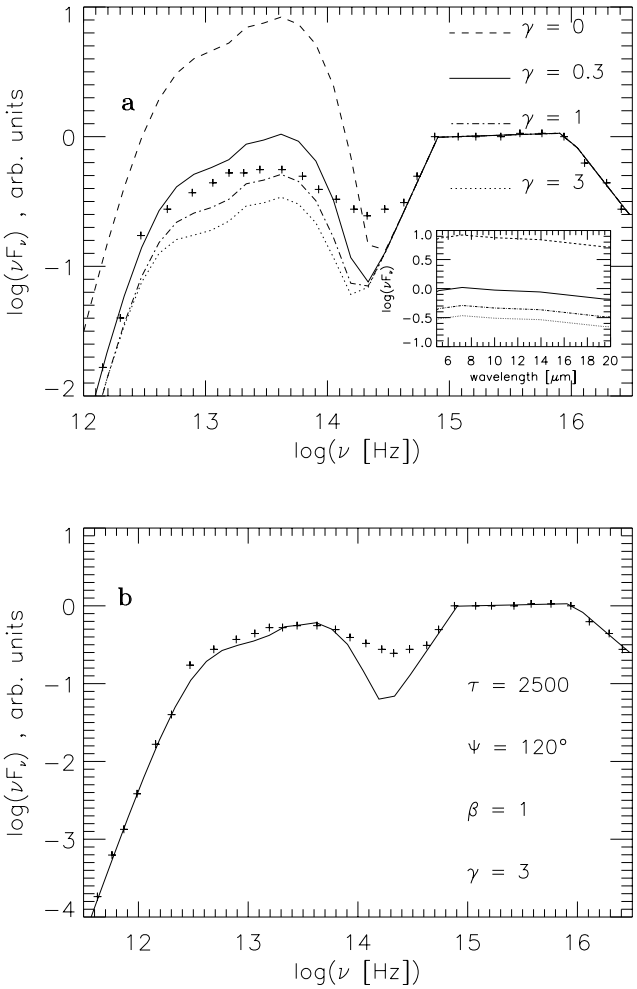

Fig. 4. a Face-on SEDs for dust tori with $\tau_{200\mathrm{nm}}$ = 3000 and β = 1 for different anisotropy factors γ. In the small figure we show a magnifikation of the wavelength region around 10 μm. **b** SED for "best fit" torus model (torus dust mass $M_{dust} = 4 \cdot 10^6\,\mathrm{M}_\odot$). The '+' signs indicate the observed data from Sanders et al. (1989). For reference, the silicate feature would appears at $10\mu\mathrm{m} \approx log(\nu) = 13.4$

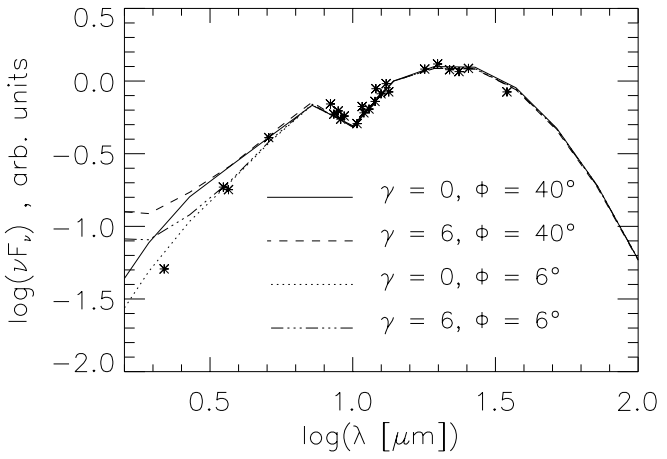

Fig. 5. SEDs for two different anisotropy factors γ and for two different viewing angles Φ, for lines of sight where the central source is obscured (model parameters: $\tau_{200nm} = 50$, $\beta = 1$, $\Psi = 120°$). To enable the comparison of our results with the observed data for NGC 1068 (Rieke & Low (1975) and Roche et al. (1991), indicated by the asterisks) we scaled our SEDs and the data to have the same IR luminosity.

In Fig. 4**b** we present a model which fits the observed average broad band emission of PG quasars (Sanders et al. 1989) quite good. It shows the same UV to IR ratio as the observed data and no silicate feature is present at all. Like all other models presented in this paper, the SED shows a lack of emission in the wavelength interval of about 3...0.8 μm ($log(\nu)$ = 14...14.6). As already mentioned in Sect. 4.1, this seems to reflect the simplicity of our model assumptions and the lack of emission from transiently heated particles.

These results contradict the predictions of Efstathiou & Rowan-Robinson (1995) and Stenholm (1995) who postulated only little influence on the spectra due to the angular distribution of radiation of the central source. We demonstrated that an anisotropically radiating central source gives better agreement with the observations of dust emission of AGN seen face-on.

4.3.1. Seyfert 2 AGN - a viewing angle effect ?

To check briefly if the assumption of anisotropic central radiation sources matches to the unified theory for AGN, where the different SEDs are mainly due to different viewing angles, we also calculated the SEDs of our tori models for additional viewing angles where the line of sight intersects the dust torus. In Fig. 5 we present the SEDs obtained for a torus with an optical depth $\tau_{200nm} = 50$ as such a value of optical depth is required from the observations (Rieke & Low 1975, Roche et al. 1991) and modeling of NGC 1068 (Efstathiou et al. 1995), a typical Seyfert 2 AGN. For comparison, the observed data for NGC 1068 are also shown in Fig. 5. Although our aim was not to explicitly fit the data of NGC 1068, our results coincide quite well with the observations. Only for wavelengths shorter than 5 μm significant differences show up. As this part of the SED is mainly influenced by emission and scattering from the conical surface of the torus it is very sensitive to changes of the torus opening angle and of the viewing angle. Recent detailed modeling of NGC 1068, reported by Efstathiou et al. (1995), support the need for anisotropy in the source radiation and indicate a viewing angle $\leq 40°$ for NGC1068, whereas the opening angle of the torus might be much smaller than in our model. However, our model can reproduce the main characteristics of Seyfert 2 AGN, the main shape of the IR part of the SED and the silicate feature in absorption, in support of the unified theory of AGN.

5. Conclusions

We described an accelerated version of the radiative transfer code of MH for axisymmetric dust configurations. With a flared disk geometry, we investigated the model spectra of dust tori surrounding AGN for a wide region of the parameter space. Our results show that flared disk models with isotropically radiating central sources have problems in explaining both the observed UV to IR flux ratio and the absence of a silicate emission feature. On the other hand, the models with an anisotropic source which fit better into the unified theory for AGN producing spectra which look similar to the observed ones and showing no or almost no silicate feature.

In contrast to other authors (Laor & Draine 1993, Granato & Danese 1994) we had not to introduce grain depletion mechanisms to lower the amount of small silicate grains in order to find agreement with the observations. We also see no need for compact cores (Pier & Krolik 1993), but these might be necessary just due to a different model geometry. There is also no necessity to switch from flared disks to tapered disks (Stenholm 1995, Efstathiou & Rowan-Robinson 1995) to explain the observed AGN spectra if anisotropic central sources are used. On the other hand, anisotropic sources in combination with spherically symmetric dust envelopes fail to fit the observations (Loska et al. 1993). Our results demonstrate, that together with anisotropically radiating central sources, optically thick dust tori with a flared disk geometry, opening angles of about 90°, and density distributions $\rho(r) \propto r^{-1}$ give a reasonable explanation for the observed spectra of AGN seen face-on. Furthermore, we found that dust tori with anisotropic sources are consistent with the unified theory for AGN as they can also reproduce the main characteristics in the SED of typical Seyfert 2 AGN, where the central source is obscured by the dust torus. The presented models avoid the production of the silicate emission feature for AGN of type 1 (torus seen face-on), but keep the feature in absorption for AGN of type 2 (torus seen edge-on). The fact that very high optical depths $\tau_{200nm} > 1000$ are necessary to fit the average broad band emission of PG quasar, whereas much lower optical depths $\tau_{200nm} \approx 50$ are required for Seyfert 2 (i.e. NGC1068) may reflect the simplicity of our torus model, where the density distribution depends only on the radial coordinate.

Acknowledgements. We like to thank L.Danese for his helpful comments that led to an improvement of this paper.

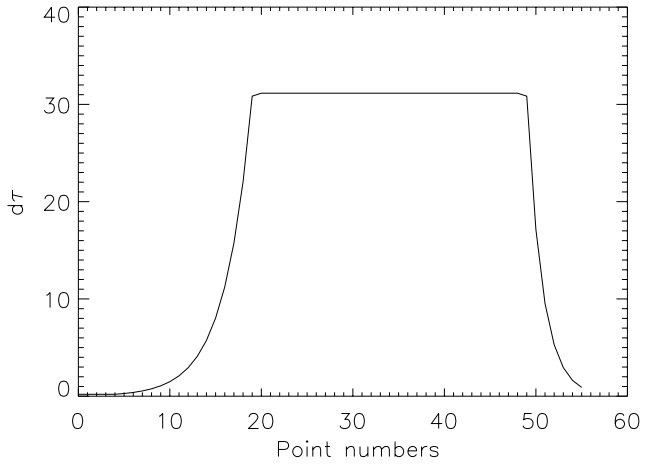

Fig. 6. Optical depth increment dτ between the radial points vs. grid point number for a model with $\tau_{200\mathrm{nm}} = 1000$

Table 3. Comparison of needed CPU time in minutes per 2D-iteration for the original MH and the improved ray-tracing algorithm (bold font). N: number of radial grid points

$\rho(r) \propto r^0$				
$\tau_{550\mathrm{nm}}$	100	500	1000	2000
N, time	83 (8.5)	78 (7)	98 (12.5)	142 (32.5)
	64 (3.6)	**69 (4.0)**	**69 (4.0)**	**69 (4.0)**
$\rho(r) \propto r^{-1}$				
$\tau_{550\mathrm{nm}}$	100	500	1000	2000
N, time	84 (8.5)	106 (15)	117 (19)	154 (41)
	45 (1.7)	**59 (3.0)**	**62 (3.5)**	**66 (3.7)**
$\rho(r) \propto r^{-2}$				
$\tau_{550\mathrm{nm}}$	100	500	1000	2000
N, time	111 (16)	121 (20)	140 (32.5)	179 (60.0)
	54 (2.5)	**56 (2.7)**	**62 (3.5)**	**68 (4.0)**

Appendix A

A.1. Grid definition

We use a radial grid that is directly related to the optical depth τ of the torus. The grid points are equidistantly spaced in τ in the middle of the grid and equidistantly spaced in $\log \tau$ at its edges, as shown in Fig. 6.

Before using this adapted grid, the grid was constructed using no physical information from the current torus model, being simply equidistantly spaced in logarithm of r. This simpler approach is much easier to program and has been used by many authors. However, for our models with extremely high optical depth, the adapted grid needs less points to reach the same level of numerical accuracy and, therefore, the program is faster (Sect. 5).

A.2. Ray tracer

The most time-consuming part of the radiative transfer code is the integration of Eq. (1) for all radial points and all given directions. This is done using the formal solution of Eq. (1) (to simplify matters only the ray with $\mu = 1$ is considered in the formulas below):

$$I_\nu(r_2) = \int_{\tau(r_1)}^{\tau(r_2)} S_\nu(\tau)\, e^{-\tau}\, \mathrm{d}\tau + I_\nu(r_1)\, e^{-\Delta\tau} \tag{A1}$$

where the optical depth is defined by

$$\tau(r) := \tau_\nu(r) = \int_{R_{\min}}^{r} \sigma_\nu^{\mathrm{ext}}(s)\, \mathrm{d}s\,, \tag{A2}$$

$$\Delta\tau = \tau(r_2) - \tau(r_1)\,. \tag{A3}$$

In the version of the program described by MH, the integral over the source function S was computed assuming that S is constant between two grid points. To approximately fulfill this assumption, a lot of grid points are required for high optical depths ($\tau_{550\mathrm{nm}} \gg 100$).

In the new version of the code, we use the method of weighted mean parabolas of Kurucz (1970) assuming a locally quadratic behavior of the source function in order to increase the accuracy of the numerical integration of Eq. A1. The integration of the source function from the radial point i to the point $i + 1$ can now be done straightforward:

$$\begin{aligned}
&\int_0^{\Delta\tau_i} S_\nu(x)\; e^{-x}\, \mathrm{d}x \\
&= \int_0^{\Delta\tau_i} (ax^2 + bx + c)\, e^{-x}\, \mathrm{d}x \\
&= -e^{-\Delta\tau_i}\; \left[c + b\,(\Delta\tau_i + 1) + a\,([\Delta\tau_i + 1]^2 + 1)\right] \\
&\quad + 2a + b + c\,, \qquad \text{(A4)}
\end{aligned}$$

(A5)

where the coefficients *a, b*, and *c* of the quadratic polynomial are functions of $S_\nu(r_{i-1})$,...,$S_\nu(r_{i+2})$.

After an additional complete rewriting of the ray-tracing part of the program, we are now able to perform calculations with a much fewer number of grid points and to apply a better ray-tracing algorithm, which results in a big gain in CPU time (see Table 3).

A.3. Accuracy and CPU time comparisons

To measure the gain of CPU time due to the modifications of the program of MH, we calculated 12 models with the modified and the original code. The chosen values for optical depth and the density power-law index cover all AGN tori models presented in this paper and most of the models calculated by MH.

The calculations for Table 3 were done for spherically-symmetric dust envelopes and flared dust disks around a B-type star ($T_{\rm eff}$ = 10^4 K) using 40 frequencies (wavelengths from 10 nm to 1 mm) equidistantly spaced in logarithm.

The major constraint that determined the number of radial points (and, therefore, the CPU time) was our demand that at any point in the envelope, the conservation of energy should be guaranteed with a relative deviation of less than 10 %. With the version of the code of MH, it was not always possible to reach that goal. Most of the models with optical depth $\tau_{550\rm nm} > 100$ for the density distributions $\rho(r) \propto r^{-1}$ and $\rho(r) \propto r^{-2}$ showed locally relative deviations up to 20 %. Even finer grids with more radial points could not lower the values.

The CPU times in Table 3 are given for the corresponding torus models with the opening angle of 90° and the same values for the internal parameters in both versions of the code. All computations were done on a DEC-Alpha 3000/500 workstation with a peak performance of 30 Mflop.

References

Antonucci R.R., 1993, ARA&A 31, 473
Antonucci R.R., Miller J.S., 1985, ApJ 297, 621
Dorschner J., Begemann B., Henning Th., Jäger C., Mutschke H., 1995, A&A 300, 503
Draine B.T, 1985, ApJS, 57, 587
Efstathiou A., Rowan-Robinson M., 1995, MNRAS 273, 649
Efstathiou A., Hough J.H., Young S., 1995, MNRAS 277,1134
Fischer O., 1995, Rev.Mod.Astron. 8,103
Gledhill T.M., Chrysostomou A., Hough J.H., 1996, MNRAS 282,1418
Goodrich W.R., 1995, ApJ 440, 141
Granato G.L., Danese L., 1994, MNRAS 268, 235
Guhathakurta P., Draine B.T., 1989, ApJ 345, 230
Harms R.J., Ford H.C., Tsvetanov Z.I. et al., 1994, ApJ 435, L35
Heckman T.M., 1995, ApJ 446, 101
Henning Th., Stognienko R., 1996, A&A 311, 291
Henning Th., Michel B., Stognienko R., 1995, PS&SS 43, 1333
Jäger C., Mutschke H., Begemann B., Dorschner J., Henning Th., 1994, A&A 292, 641
Jaffe W., Ford H.C., Ferrarese L., van den Bosch F., O'Connel R.W., 1993, Nat 364, 213
Krügel E., Siebenmorgen R., 1994, A&A 282, 407
Kurucz R.L., 1970, Smithsonian Ap. Obs. Spec. Rept. No 309
Laor A., Draine B.T., 1993, ApJ 402, 441
Lawrence A., 1987, PASP 99,309
Lawrence A., 1991, MNRAS 252, 586
Lawrence A., Elvis M., 1982, ApJ 256, 410
Lenzuni P., Gail H.P., Henning Th., 1995, ApJ 447, 848
Loska Z., Szczerba R., Czerny B., 1993, MNRAS 261, 63
Mathis J.S., Rumpl W., Nordsieck K.H., 1977, ApJ 215, 425
Men'shchikov A.B., Henning Th., 1997, A&A, 318, 879
Miller J.S., Goodrich R.W., 1990, ApJ 355, 456
Miller J.S., Goodrich R.W., Mathews W.G., 1991, ApJ 378, 47
Ossenkopf V., Henning Th., 1994, A&A 291, 943
Pier E.A., Krolik J.H., 1992, ApJ 401, 99
Pier E.A., Krolik J.H., 1993, ApJ 418, 673
Preibisch Th., Ossenkopf V., Yorke H., Henning Th., 1993, A&A 279, 577
Preibisch Th., Sonnhalter C., Yorke H.W., 1995, A&A 299, 144
Rees M.J., 1984, ARA&A 22, 471
Rieke G.H., Low F.J., 1975, ApJ 199, L13
Roche P.F., Aitken D.K., Smith C.H., Ward M.J., 1991, MNRAS 248, 606
Rowan-Robinson M., 1992, MNRAS 258, 787
Sanders D.B., Phinney E.S., Neugebauer G., Soifer B.T., Matyhews K., 1989, ApJ 347, 29
Scarrott S.M., Rolph C.D., Wolstencroft R.W., Tadhunter C.N., 1991, MNRAS 249, 16p
Stenholm L., 1995, A&A 290, 393
Storchi–Bergman T., Wilson A.S., Baldwin J.A., 1992, ApJ 396, 45
Tran H.D., 1995, ApJ 440, 597
Urry C.M., Padovani P., 1995, PASP 107, 803
Young S., Packham C., Hough J.H., Efstathiou A., 1996, MNRAS 283, L1

This article was processed by the author using Springer-Verlag LaTeX A&A style file *L-AA* version 3.